Quantum Threshold Voltage Modeling of Short Channel Quad Gate Silicon Nanowire Transistor

P. Rakesh Kumar and Santanu Mahapatra, *Member, IEEE*

***Abstract*—In this paper, a physically based analytical quantum linear threshold voltage model for short channel quad gate MOSFETs is developed. The proposed model, which is suitable for circuit simulation, is based on the analytical solution of 3-D Poisson and 2-D Schrödinger equation. Proposed model is fully validated against the professional numerical device simulator for a wide range of device geometries and also used to analyze the effect of geometry variation on the threshold voltage.**

***Index Terms*—CMOS, compact modeling, multigate transistors, quantum effects.**

I. Introduction

QUAD GATE MOSFETs has attracted much attention for downscaling CMOS technology up to 10 nm channel length due to its maximum gate control over the channel and high current drive capability [1]. In such transistors, the short channel effect (SCE) is controlled by the device geometry, and hence, an undoped (or lightly doped) ultrathin body is used to sustain the channel. Since the quantization of electron energy cannot be ignored in such ultrathin body devices, it is extremely important to consider quantum effects in their threshold voltage models. To the best of our knowledge, quantum threshold voltage model for short channel devices have not yet been reported apart from the recent long channel model, which is implicit in nature [2]. In this paper, we propose a physically based closed form quantum linear threshold voltage model, which is applicable for ultrathin and ultrashort channel quad gate devices and does not contain any unphysical fitting parameter. The 3-D Poisson equation and 2-D Schrödinger equation (with square potential well approximation) are solved in the weak inversion region to obtain the threshold voltage model. It is shown that electron distribution in energy subbands in the quad gate MOSFET is quite different from the bulk and double gate MOSFET. The proposed models are validated against the numerical device simulator Atlas [3] for different device architecture. The effect of effective mass and geometry variation on the threshold voltage is also studied using the proposed model.

Manuscript received June 30, 2009. Date of publication September 29, 2009; date of current version January 26, 2011. This work was funded by Department of Science and Technology, India under Grant SR/S3/EECE/047/2008. The review of this paper was arranged by Associate Editor M. Anantram.

The authors are with the Nanoscale Device Research Laboratory, Centre for Electronics Design and Technology, Indian Institute of Science, Bengaluru, Karnataka 560012, India (e-mail: prakesh@cedt.iisc.ernet.in; santanu@cedt.iisc.ernet.in).

Color versions of one or more of the figures in this paper are available online at http://ieeexplore.ieee.org.

Digital Object Identifier 10.1109/TNANO.2009.2033380

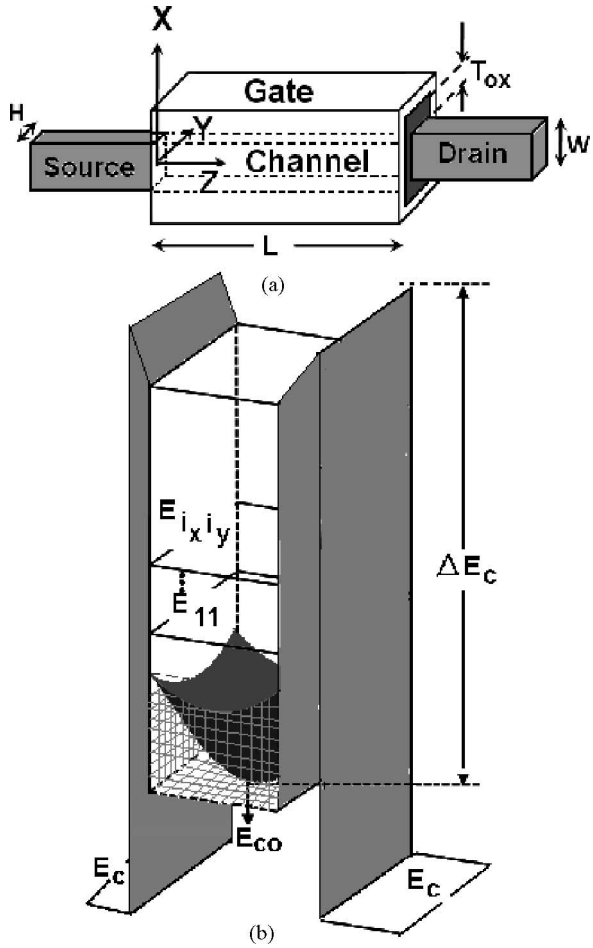

Fig. 1. (a) Schematic of quad gate transistor. (b) Band diagram perpendicular to the gate.

II. Model Development

A. Potential Modeling

In ultrathin devices, the quantization of electron energy due to structural confinement becomes significant. Hence, the Poisson–Schrödinger equations has to be consistently solved to obtain potential distribution and inversion charge density. However, in the weak inversion regime, one can approximate the Poisson equation as the Laplace equation by ignoring the inversion charge density, and hence, decouple the two equations. In the development of threshold voltage models, we have also taken the parabolic band approximation. We have used mid gap metals for the gates. Fig. 1 shows the schematic diagram of an undoped (or lightly doped) quad gate MOSFET. The same voltage is

applied to all the four gates. In both the insulator and silicon region, the Poisson (Laplace) equation becomes

$$\frac{\delta^2\Phi}{\delta x^2}+\frac{\delta^2\Phi}{\delta y^2}+\frac{\delta^2\Phi}{\delta z^2}=0 \tag{1}$$

with the boundary conditions

$$\Phi(x,-H/2-T_{\rm ox},z)=V_g \tag{2}$$

$$\Phi(-W/2-T_{\rm ox},y,z)=V_g \tag{3}$$

$$\frac{\delta\phi}{\delta x}|_{x=0}=0 \tag{4}$$

$$\frac{\delta\phi}{\delta y}|_{y=0}=0 \tag{5}$$

$$\Phi(x,y,0)=V_{\rm bi} \tag{6}$$

$$\Phi(x,y,L)=V_{\rm bi}+V_{\rm ds}\simeq V_{\rm bi}\ \text{for low}\ V_{\rm ds}. \tag{7}$$

Here, Φ is the potential, $V_{\rm bi}$ is the built-in potential of a n^+-i diode, V_g is the gate potential and $V_{\rm ds}$ is the drain to source voltage, H and W are the height and width of the silicon film, $T_{\rm ox}$ is the gate oxide thickness, and L is the channel length, respectively. 3-D numerical simulation results show that in the insulator region the potential can be approximated as a linear function. We further neglect the corner effects. The potential inside the insulator region can then be expressed by linear interpolation as

$$\Phi(x,y,0)=\frac{V_g-V_{\rm bi}}{T_{\rm ox}}\left(x-\frac{W}{2}\right)+V_{\rm bi}\quad \text{for}\ \frac{W}{2}<x<\frac{W}{2}+T_{\rm ox}\ \text{and}\ 0<y<\frac{H}{2} \tag{8}$$

$$\Phi(x,y,0)=\frac{V_g-V_{\rm bi}}{T_{\rm ox}}\left(y-\frac{H}{2}\right)+V_{\rm bi}\quad \text{for}\ 0<x<\frac{W}{2}\ \text{and}\ \frac{H}{2}<y<\frac{H}{2}+T_{\rm ox}. \tag{9}$$

Using superposition, the potential can be written as

$$\Phi(x,y,z)=\upsilon(x,y)+u_L(x,y,z)+u_R(x,y,z). \tag{10}$$

Here, $\upsilon(x,y)$ is the long channel potential, which satisfy the boundary conditions (2) and (3). $\upsilon(x,y)$ should also satisfy the dielectric boundary conditions, namely $\epsilon(\delta\upsilon/\delta x)$ and $\upsilon(x,y)$ are continuous at $x=W/2$, and $\epsilon(\delta\upsilon/\delta y)$ and $\upsilon(x,y)$ are continuous at $y=H/2$. For quad gate MOSFET, where all the gates have same voltage, we have $\upsilon(x,y)=V_g$. Potentials $u_L(x,y,z)$ and $u_R(x,y,z)$ capture SCE and satisfies the boundary conditions (6) and (7). Potentials $u_L(x,y,z)$ and $u_R(x,y,z)$ can be written as

$$u_L=\sum_n\sum_m a_{\rm Tnm}\sin\left(\lambda_n\left(x-\frac{W}{2}-T_{\rm ox}\right)\right)\cos(\mu_m y)\times\frac{\sinh(\sigma_{\rm nm}(L-z))}{\sinh(\sigma_{\rm nm}L)}\quad \text{for}\ \frac{W}{2}<x<\frac{W}{2}+T_{\rm ox}\ \text{and}\ 0<y<\frac{H}{2} \tag{11}$$

$$u_L=\sum_n\sum_m a_{\rm bnm}\cos(\lambda_n x)\sin\left(\mu_m\left(y-\frac{H}{2}-T_{\rm ox}\right)\right)\times\frac{\sinh(\sigma_{\rm nm}(L-z))}{\sinh(\sigma_{\rm nm}L)}\quad \text{for}\ 0<x<\frac{W}{2}\ \text{and}\ \frac{H}{2}<y<\frac{H}{2}+T_{\rm ox} \tag{12}$$

$$u_L=\sum_n\sum_m a_{\rm nm}\cos(\lambda_n x)\cos(\mu_m y)\times\frac{\sinh(\sigma_{\rm nm}(L-z))}{\sinh(\sigma_{\rm nm}L)}\quad \text{for}\ 0<x<\frac{W}{2}\ \text{and}\ 0<y<\frac{H}{2} \tag{13}$$

$$u_R=\sum_n\sum_m b_{\rm Tnm}\sin\left(\lambda_n\left(x-\frac{W}{2}-T_{\rm ox}\right)\right)\cos(\mu_m y)\times\frac{\sinh(\sigma_{\rm nm}z)}{\sinh(\sigma_{\rm nm}L)}\quad \text{for}\ \frac{W}{2}<x<\frac{W}{2}+T_{\rm ox}\ \text{and}\ 0<y<\frac{H}{2} \tag{14}$$

$$u_R=\sum_n\sum_m b_{\rm bnm}\cos(\lambda_n x)\sin\left(\mu_m\left(y-\frac{H}{2}-T_{\rm ox}\right)\right)\times\frac{\sinh(\sigma_{\rm nm}z)}{\sinh(\sigma_{\rm nm}L)}\quad \text{for}\ 0<x<\frac{W}{2}\ \text{and}\ \frac{H}{2}<y<\frac{H}{2}+T_{\rm ox} \tag{15}$$

$$u_R=\sum_n\sum_m b_{\rm nm}\cos(\lambda_n x)\cos(\mu_m y)\times\frac{\sinh(\sigma_{\rm nm}z)}{\sinh(\sigma_{\rm nm}L)}\quad \text{for}\ 0<x<\frac{W}{2}\ \text{and}\ 0<y<\frac{H}{2}. \tag{16}$$

Here, $a_{\rm Tnm}, a_{\rm bnm}, a_{\rm nm}, b_{\rm Tnm}, b_{\rm bnm}$, and $b_{\rm nm}$ are the constants to be obtained from the boundary conditions (2) and (3). $\sigma_{\rm nm}$ is given by the following expression:

$$\sigma_{\rm nm}=\sqrt{\lambda_n^2+\mu_m^2}. \tag{17}$$

The Poisson equation requires Φ and $\epsilon(\delta\Phi/\delta x)$ be continuous in the x-direction, and Φ and $\epsilon(\delta\Phi/\delta y)$ be continuous in the y-direction. The dielectric boundary conditions at the two silicon–insulator interfaces requires u_L and $\epsilon(\delta u_L/\delta x)$ be continuous at $x=W/2$, and u_L and $\epsilon(\delta u_L/\delta y)$ be continuous at $y=H/2$. Applying continuity in (11) and (13) along x-direction we get

$$-a_{\rm Tnm}\sin(\lambda_n T_{\rm ox})=a_{\rm nm}\cos\left(\frac{\lambda_n W}{2}\right) \tag{18}$$

$$a_{\rm Tnm}\epsilon_{\rm ox}\lambda_n\cos(\lambda_n T_{\rm ox})=-a_{\rm nm}\epsilon_{\rm si}\lambda_n\sin\left(\frac{\lambda_n W}{2}\right). \tag{19}$$

Taking the ratio of the above two equations, we get λ_n from the following equation:

$$\epsilon_{\rm si}\tan\left(\lambda_n T_{\rm ox}\right)-\epsilon_{\rm ox}\cot\left(\frac{\lambda_n T}{2}\right)=0. \tag{20}$$

Similarly, applying continuity in (12) and (13) along y-direction and taking their ratio, we get a equation for μ_m as

$$\epsilon_{\rm si}\tan\left(\mu_m T_{\rm ox}\right)-\epsilon_{\rm ox}\cot\left(\frac{\mu_m H}{2}\right)=0. \tag{21}$$

Note that λ_n and μ_m depends only on the device parameters. Now u_L can be rewritten as $s_{\rm nm}U_{\rm Lnm}$, where

$$u_{\rm Lnm}=\alpha_{\rm nm}\sin\left(\lambda_n\left(x-\frac{W}{2}-T_{\rm ox}\right)\right)\cos\left(\mu_m y\right)\times\frac{\sinh\left(\sigma_{\rm nm}(L-z)\right)}{\sinh\left(\sigma_{\rm nm}L\right)}\quad\text{for }\frac{W}{2}<x<\frac{W}{2}+T_{\rm ox}\text{ and }0<y<\frac{H}{2} \tag{22}$$

$$u_{\rm Lnm}=\beta_{\rm nm}\cos\left(\lambda_n x\right)\sin\left(\mu_m\left(y-\frac{H}{2}-T_{\rm ox}\right)\right)\times\frac{\sinh\left(\sigma_{\rm nm}(L-z)\right)}{\sinh\left(\sigma_{\rm nm}L\right)}\quad\text{for }0<x<\frac{W}{2}\text{ and }\frac{H}{2}<y<\frac{H}{2}+T_{\rm ox} \tag{23}$$

$$u_{\rm Lnm}=\gamma_{\rm nm}\cos\left(\lambda_n x\right)\cos\left(\mu_m y\right)\frac{\sinh\left(\sigma_{\rm nm}(L-z)\right)}{\sinh\left(\sigma_{\rm nm}L\right)}\quad\text{for }0<x<\frac{W}{2}\text{ and }0<y<\frac{H}{2}. \tag{24}$$

Eigen functions $u_{\rm Lnm}$ as defined by (22)–(24) are not orthogonal to each other. In order to evaluate the coefficient $s_{\rm nm}$, we need to construct a corresponding conjugate function set g_n. It turns out that $g_{\rm nm}$ can be made from the same set of functions as in (22)–(24) by choosing different multipliers in different regions and constants $\alpha_{\rm nm}$, $\beta_{\rm nm}$, and $\gamma_{\rm nm}$ appropriately. The conjugate function set $g_{\rm nm}$ is found as

$$g_{\rm nm}=\frac{\epsilon_{\rm ox}}{2\epsilon_{\rm si}}\frac{\sin\left(\lambda_n\left(x-W/2-T_{\rm ox}\right)\right)\cos\left(\mu_m y\right)}{\sin\left(\lambda_n T_{\rm ox}\right)\cos\left((\mu_m H)/2\right)}\quad\text{for }\frac{W}{2}<x<\frac{W}{2}+T_{\rm ox}\text{ and }0<y<\frac{H}{2} \tag{25}$$

$$g_{\rm nm}=\frac{\epsilon_{\rm ox}}{2\epsilon_{\rm si}}\frac{\cos\left(\lambda_n x\right)\sin\left(\mu_m\left(y-H/2-T_{\rm ox}\right)\right)}{\cos\left((\lambda_n W)/2\right)\sin\left(\mu_m T_{\rm ox}\right)}\quad\text{for }0<x<\frac{W}{2}\text{ and }\frac{H}{2}<y<\frac{H}{2}+T_{\rm ox} \tag{26}$$

$$g_{\rm nm}=-\frac{\cos\left(\lambda_n x\right)\cos\left(\mu_m y\right)}{\cos\left((\lambda_n W)/2\right)\cos\left((\mu_m H)/2\right)}\quad\text{for }0<x<\frac{W}{2}\text{ and }0<y<\frac{H}{2}. \tag{27}$$

The constants $\alpha_{\rm nm}$, $\beta_{\rm nm}$, and $\gamma_{\rm nm}$ are given as

$$\alpha_{\rm nm}=\cos\left(\frac{\lambda_n W}{2}\right)\sin\left(\mu_m T_{\rm ox}\right) \tag{28}$$

$$\beta_{\rm nm}=\cos\left(\frac{\mu_m H}{2}\right)\sin\left(\lambda_n T_{\rm ox}\right) \tag{29}$$

$$\gamma_{\rm nm}=-\sin\left(\lambda_n T_{\rm ox}\right)\sin\left(\mu_m T_{\rm ox}\right). \tag{30}$$

Similarly, u_R can be written as $t_{\rm nm}u_{\rm Rnm}$, where $u_{\rm Rnm}$ is given as

$$u_{\rm Rnm}=\alpha_{\rm nm}\sin\left(\lambda_n\left(x-\frac{W}{2}-T_{\rm ox}\right)\right)\cos\left(\mu_m y\right)\times\frac{\sinh\left(\sigma_{\rm nm}z\right)}{\sinh\left(\sigma_{\rm nm}L\right)}\quad\text{for }\frac{W}{2}<x<\frac{W}{2}+T_{\rm ox}\text{ and }0<y<\frac{H}{2} \tag{31}$$

$$u_{\rm Rnm}=\beta_{\rm nm}\cos\left(\lambda_n x\right)\sin\left(\mu_m\left(y-\frac{H}{2}-T_{\rm ox}\right)\right)\times\frac{\sinh\left(\sigma_{\rm nm}z\right)}{\sinh\left(\sigma_{\rm nm}L\right)}\quad\text{for }0<x<\frac{W}{2}\text{ and }\frac{H}{2}<y<\frac{H}{2}+T_{\rm ox} \tag{32}$$

$$u_{\rm Rnm}=\gamma_{\rm nm}\cos\left(\lambda_n x\right)\cos\left(\mu_m y\right)\frac{\sinh\left(\sigma_{\rm nm}z\right)}{\sinh\left(\sigma_{\rm nm}L\right)}\quad\text{for }0<x<\frac{W}{2}\text{ and }0<y<\frac{H}{2} \tag{33}$$

$u_{\rm Lnm}$ at $x=W/2$ and $y=H/2$ from (22) is given as

$$u_{\rm Lnm}=-\alpha_{\rm nm}\sin\left(\lambda_n T_{\rm ox}\right)\cos\left(\mu_m\frac{H}{2}\right)=-\sin\left(\mu_m T_{\rm ox}\right)\sin\left(\lambda_n T_{\rm ox}\right)\cos\left(\mu_m\frac{H}{2}\right)\cos\left(\lambda_n\frac{W}{2}\right) \tag{34}$$

$u_{\rm Lnm}$ at $x=W/2$ and $y=H/2$ from (23) is given as

$$u_{\rm Lnm}=-\beta_{\rm nm}\sin\left(\mu_m T_{\rm ox}\right)\cos\left(\lambda_n\frac{W}{2}\right)=-\sin\left(\mu_m T_{\rm ox}\right)\sin\left(\lambda_n T_{\rm ox}\right)\cos\left(\mu_m\frac{H}{2}\right)\cos\left(\lambda_n\frac{W}{2}\right) \tag{35}$$

$u_{\rm Lnm}$ at $x=W/2$ and $y=H/2$ from (24) is given as

$$u_{\rm Lnm}=-\gamma_{\rm nm}\cos\left(\mu_m\frac{H}{2}\right)\cos\left(\lambda_n\frac{W}{2}\right)=-\sin\left(\mu_m T_{\rm ox}\right)\sin\left(\lambda_n T_{\rm ox}\right)\cos\left(\mu_m\frac{H}{2}\right)\cos\left(\lambda_n\frac{W}{2}\right). \tag{36}$$

Since, potential is given by $\sum_n\sum_m s_{\rm snm}u_{\rm Lnm}$ and from (34)–(36), it is seen that $u_{\rm Lnm}$ gives the same value at the

corner, potential is continuous at the corner. By multiplying (22)–(24) with the corresponding conjugate functions (25)–(27) and integrating, the coefficients $s_{\rm nm}$ can be obtained as

$$s_{\rm nm}=\frac{\int_0^{H+T_{\rm ox}}\int_0^{W+T_{\rm ox}}\left(\Phi(x,y,0)-\upsilon(x,y)\right)g_{\rm nm}(x,y)\,dxdy}{\int_0^{H+T_{\rm ox}}\int_0^{W+T_{\rm ox}}u_{\rm Lnm}(x,y,0)g_{\rm nm}(x,y)\,dxdy}$$
$$=(V_g-V_{\rm bi})\frac{\Omega_{\rm nm}}{\zeta_{\rm nm}}. \tag{37}$$

Similarly, $t_{\rm nm}$ can be obtained as

$$t_{\rm nm}=\frac{\int_0^{H+T_{\rm ox}}\int_0^{W+T_{\rm ox}}\left(\Phi(x,y,L)-\upsilon(x,y)\right)g_{\rm nm}(x,y)\,dxdy}{\int_0^{H+T_{\rm ox}}\int_0^{W+T_{\rm ox}}u_{\rm Rnm}(x,y,L)g_{\rm nm}(x,y)\,dxdy}$$
$$=(V_g-V_{\rm bi}-V_{\rm ds})\frac{\Omega_{\rm nm}}{\zeta_{\rm nm}} \tag{38}$$

where $\Omega_{\rm nm}$ and $\zeta_{\rm nm}$ are given by the following equations:

$$\Omega_{\rm nm}=\frac{\epsilon_{\rm ox}\mu_m\tan\left((\mu_m H)/2\right)+\epsilon_{\rm ox}\lambda_n\tan\left((\lambda_n W)/2\right)}{2\epsilon_{\rm si}T_{\rm ox}\mu_m^2\lambda_n^2}$$
$$-\frac{2}{\mu_m\lambda_n}\tan\left(\frac{\mu_m H}{2}\right)\tan\left(\frac{\lambda_n W}{2}\right) \tag{39}$$

$$\zeta_{\rm nm}=\frac{\sin(\mu_m T_{\rm ox})}{16\cos\left((\mu_m H)/2\right)}\left(H+\frac{\sin(\mu_m H)}{\mu_m}\right)$$
$$\times\left(\frac{\epsilon_{\rm ox}T_{\rm ox}\cos\left((\lambda_n W)/2\right)}{\epsilon_{\rm si}\sin(\lambda_n T_{\rm ox})}+\frac{W\sin(\lambda_n T_{\rm ox})}{2\cos\left((\lambda_n W)/2\right)}\right)$$
$$+\frac{\sin(\lambda_n T_{\rm ox})}{16\cos\left((\lambda_n W)/2\right)}\left(W+\frac{\sin(\lambda_n W)}{\lambda_n}\right)$$
$$\times\left(\frac{\epsilon_{\rm ox}T_{\rm ox}\cos\left((\mu_m H)/2\right)}{\epsilon_{\rm si}\sin(\mu_m T_{\rm ox})}+\frac{H\sin(\mu_m T_{\rm ox})}{2\cos\left((\mu_m H)/2\right)}\right). \tag{40}$$

Using (10) potential in the silicon region can be written as

$$\Phi(x,y,z)=V_g+(V_g-V_{\rm bi})\sum_n\sum_m c_{\rm nm}\sinh(\sigma_{\rm nm}(L-z))$$
$$+(V_g-V_{\rm bi}-V_{\rm ds})\sum_n\sum_m\sinh(\sigma_{\rm nm}z) \tag{41}$$

where $c_{\rm nm}$ is given by

$$c_{\rm nm}(x,y)=-\frac{\Omega_{\rm nm}\gamma_{\rm nm}}{\zeta_{\rm nm}}\frac{\cos(\lambda_n x)\cos(\mu_m y)}{\sinh(\sigma_{\rm nm}L)} \tag{42}$$

B. Classical Threshold Voltage Modeling

Threshold voltage for undoped body devices is defined as the gate voltage when the integrated charge at the virtual cathode becomes equal to the critical charge (Q_T). It is found from the numerical simulation that only the first series term in (41) is sufficient to predict the potential at virtual cathode, and hence, in the further analysis only the first term is used. Classical integrated charge is obtained from (41) as

$$Q=\int_{-H/2}^{H/2}\int_{-W/2}^{W/2}qn_i e^{\left(\frac{\Phi}{U_T}\right)}\,dxdy. \tag{43}$$

Now, as Φ is a very complicated function of x and y, the above integration cannot be evaluated analytically. Therefore, the above integration can be approximated as:

$$Q\approx WHqn_i e^{\left(\frac{\Phi((3W/14),(3H/14),z_c)}{U_T}\right)}. \tag{44}$$

Here, U_T is the thermal voltage, n_i is the intrinsic carrier concentration, z_c is the virtual cathode position, which is $L/2$ for low $V_{\rm ds}$, and q is the elementary charge. Using (44) and (41), the classical threshold voltage model is obtained as shown in (45) at the bottom of the page.

C. Quantum Threshold Voltage Modeling

The potential distribution obtained in (41) is quasi-parabolic in nature in x- and y-direction [see Fig. 1(b)]. Hence, it is very difficult to solve Schrödinger equation with the potential expression given in (41). Therefore, in this paper, we approximate the actual potential well as the square potential well as shown by the checked lines in Fig. 1. In this square potential well, the bottom represents the minima of conduction band energy $(E_{\rm co})$ at the body center position $(x=0, y=0,$ and $z=z_c)$, and can be given as

$$E_{\rm co}=\frac{E_g}{2}-q\Phi(0,0,z_c). \tag{46}$$

Using the above value of potential energy (46), the Schrödinger equation becomes

$$\frac{\hbar^2}{2m_x}\frac{\delta^2\Psi}{\delta x^2}+\frac{\hbar^2}{2m_y}\frac{\delta^2\Psi}{\delta y^2}+(E-E_{\rm co})\Psi=0. \tag{47}$$

Equation (47) can be solved by standard variable separable technique [5] and its solution (Ψ) and (E) is given as

$$\Psi_{i_x i_y}(x,y)=\sqrt{\left(\frac{4}{HW}\right)}\sin\left(\frac{i_x\pi(x-(l_x/2))}{l_x}\right)$$
$$\times\sin\left(\frac{i_y\pi y-(l_y/2)}{l_y}\right) \tag{48}$$

$$E_{i_x i_y}=E_{\rm co}+\frac{\hbar^2\pi^2}{2}\left[\frac{1}{m_x}\left(\frac{i_x}{l_x}\right)^2+\frac{1}{m_y}\left(\frac{i_y}{l_y}\right)^2\right]. \tag{49}$$

Here, $\hbar=h/(2\pi)$, h is the planks constant, Ψ is the wave function, and E is the energy of the electron wave. In silicon, there are six ellipsoidal valleys with m_t and m_l as the transverse and longitudinal effective masses, and i_x and i_y are the positive natural numbers. In (48) and (49), the masses (m_x and m_y) and the lengths l_x and l_y take different values depending on the direction of quantization. For example, if masses and dimensions

$$V_{\rm TC}=\frac{U_T\ln\left(Q_T/WHqn_i\right)+2V_{\rm bi}c_{11}\left((3W/14),(3H/14)\right)\sinh(\sigma_{11}L/2)}{1+2c_{11}\left((3W/14),(3H/14)\right)\sinh(\sigma_{11}L/2)} \tag{45}$$

of the film are m_l and m_t, and W and H along the quantization direction, then in (48) and (49), m_x and m_y will assume the mass of m_t and m_l, and l_x and l_y will assume the lengths as W and H, respectively. The energy reaches a minimum for a maximum mass (49). For silicon with six energy valleys, we have thus two lower energy valleys, two middle energy valleys, and two higher energy valleys, respectively. In a special case of equal height and width of the film, the two lower energy valleys and two middle energy valleys merge producing four lower energy valleys and two higher energy valleys. Thus, the charge per unit length per valley is given by

$$Q = \sum_{i_x}\sum_{i_y} q \int_{E_{i_x i_y}}^{\infty} N_{1-\mathrm{D}} f(E) d(E). \tag{50}$$

Using $N_{1-\mathrm{D}}$ as the 1-D density of states and $f(E)$ as the Fermi-dirac function (50) leads to

$$Q = q\sum_{i_x}\sum_{i_y}\sqrt{\left(\frac{m_z}{2\pi\hbar^2}\right)}\int_{E_{i_x i_y}}^{\infty}\frac{(E-E_{i_x i_y})^{-1/2}}{1+\exp\left((E-E_F)/kT\right)}\,dE. \tag{51}$$

Here, m_z is the mass of that valley, which is perpendicular to the direction of quantization. The charge (51) is difficult to solve. However, in the weak inversion regime the Fermi level is found to be much below the conduction band energy. Hence, using Bolzmann statistics the integrated charge could be approximated as

$$\begin{aligned} Q &= q\sqrt{\left(\frac{m_z}{2\pi\hbar^2}\right)}\sum_{i_x}\sum_{i_y}\int_{E_{i_x i_y}}^{\infty}\frac{\exp\left((E_F-E)/kT\right)}{\sqrt{(E-E_{i_x i_y})}}\,dE \\ &= q\sum_{i_x}\sum_{i_y}\sqrt{\frac{m_z kT}{2\hbar^2}}\exp\left(\frac{E_F-E_{i_x i_y}}{kT}\right). \end{aligned} \tag{52}$$

Using (49) and (52), the total integrated charge at virtual cathode ($z = L/2$) is given by

$$\begin{aligned} Q = &\sum_{i_x}\sum_{i_y} q\sqrt{\frac{2kTm_t}{\hbar^2}}\exp\left(-\frac{E_{\mathrm{co}}+\kappa(i_x,i_y)}{kT}\right) \\ &+\sum_{i_x}\sum_{i_y} q\sqrt{\frac{2kTm_t}{\hbar^2}}\exp\left(-\frac{E_{\mathrm{co}}+\varpi(i_x,i_y)}{kT}\right) \\ &+\sum_{i_x}\sum_{i_y} q\sqrt{\frac{2kTm_t}{\hbar^2}}\exp\left(-\frac{E_{\mathrm{co}}+\omega(i_x,i_y)}{kT}\right) \end{aligned} \tag{53}$$

where

$$\kappa(i_x,i_y) = \frac{\hbar^2\pi^2}{2}\left[\frac{1}{m_l}\left(\frac{i_x}{W}\right)^2+\frac{1}{m_t}\left(\frac{i_y}{H}\right)^2\right] \tag{54}$$

$$\varpi(i_x,i_y) = \frac{\hbar^2\pi^2}{2}\left[\frac{1}{m_t}\left(\frac{i_x}{W}\right)^2+\frac{1}{m_l}\left(\frac{i_y}{H}\right)^2\right] \tag{55}$$

$$\omega(i_x,i_y) = \frac{\hbar^2\pi^2}{2}\left[\frac{1}{m_t}\left(\frac{i_x}{W}\right)^2+\frac{1}{m_t}\left(\frac{i_y}{H}\right)^2\right]. \tag{56}$$

However, it is seen from simulation that only one energy level is sufficient to predict the charge accurately. Hence, only one energy level is used in the further anaylsis.

Using (46) and (53) and the same definition of Q_T, the quantum threshold voltage model becomes

$$\begin{aligned} &V_{\mathrm{TQ}} \\ &= \frac{(E_g/2q)+(kT/q)\ln\left((Q_T/\rho)\right)+2V_{\mathrm{bi}}c_{11}(0,0)\sinh(\sigma_{11}L/2)}{1+2c_{11}(0,0)\sinh(\sigma_{11}L/2)} \end{aligned} \tag{57}$$

where ρ is given by

$$\begin{aligned} \rho = &q\sqrt{\frac{2kTm_t}{\hbar^2}}\left(\exp\left(-\frac{\kappa(1,1)}{kT}\right)+\exp\left(-\frac{\varpi(1,1)}{kT}\right)\right) \\ &+q\sqrt{\frac{2kTm_l}{\hbar^2}}\exp\left(-\frac{\omega(1,1)}{kT}\right). \end{aligned} \tag{58}$$

The increase in the threshold voltage due to quantum effects is obtained from (45) and (57) and is given by

$$\Delta V_T = V_{\mathrm{TQ}} - V_{\mathrm{TC}} \tag{59}$$

III. Results and Discussion

Fig. 2 shows the constant electrostatic potential contours of a quad gate transistor. We have used only one series term ($n = 1$ and $m = 1$) and 25 series terms ($n = 5$ and $m = 5$) in (10) for obtaining Fig. 2(a) and (b), respectively. It is seen from the plot that only one series term is sufficient to predict the potential at virtual cathode but one needs several terms to predict the potential close to source and drain region. Thus, the assumption of linear potential variation at the insulator boundaries is valid. It is also observed that although we neglect the insulator corners, the potential is continuous at the corners. Fig. 3 shows the quantum charge distribution plot at virtual cathode position at gate voltage 0.3 V. Color represents the model and the line represents the 3-D Atlas simulation results. Fig. 4 represents the variation of total quantum integrated charge with gate voltage. It is seen from the figure that the quantum threshold voltage increase with decrease in film thickness. This is due to increase in energy quantization with decrease in film thickness. Equation (53) is used to obtain the integrated charge with only one energy level and one series term.

Fig. 5 shows the variation of the quantum threshold voltage with width and height of the film at channel length of 20 nm. Fig. 6 shows the variation of quantum and classical threshold voltage with film height for different channel lengths at film width of 9 nm. The vertical spacing between the lines in Fig. 6 gives the SCE. It is observed that the SCE decreases slightly with energy quantization. This is due to increase in the effective band gap of silicon because of quantum effects [8]. The effect of confinement (ΔV_T), as obtained from (59) is shown in Fig. 7 as a function of device dimensions.

In literatures, no standard value is found for the threshold charge (Q_T). Some authors [7] have equated it with the thermal charge. However, we have found from the numerical simulation that the threshold voltage obtained by using the thermal charge

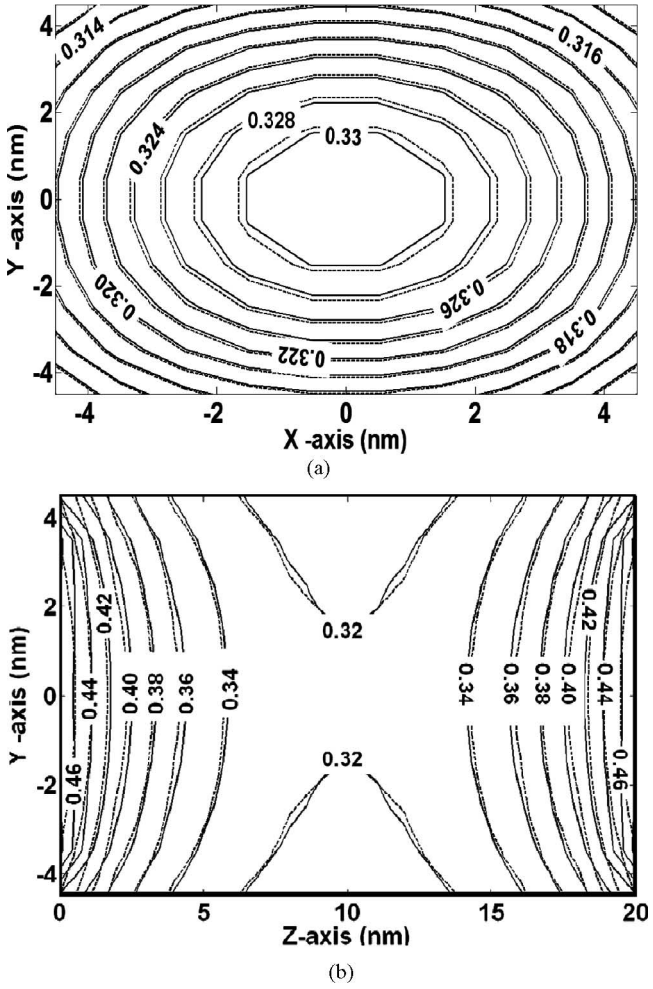

Fig. 2. Constant electrostatic potential contours based on the analytical solution (solid curves) for quad gate transistor compared with 3-D simulation results from Atlas (dashed lines). Here, $L = 20$ nm, $H = 9$ nm, $W = 9$ nm, and $V_g = 0.3$ V. (a) $X - Y$ plane at the virtual cathode ($z_c = L/2$). (b) $Y - Z$ plane at $X = 0$.

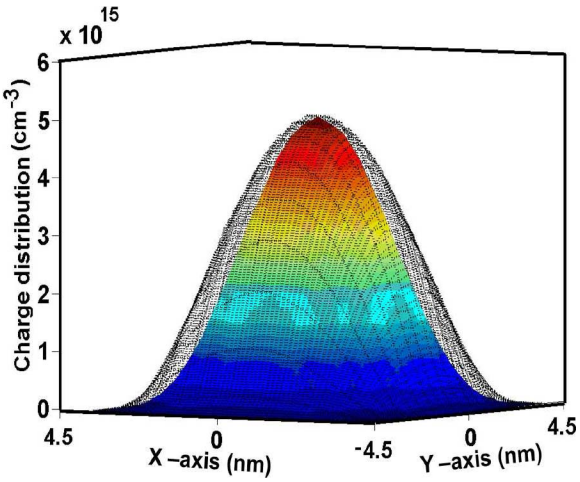

Fig. 3. Charge distribution plot at virtual cathode for QG at $V_g = 0.3$ V. Here, $H = 9$ nm, $W = 9$ nm, and $L = 20$ nm. Symbols represent Atlas simulation and lines represent the model.

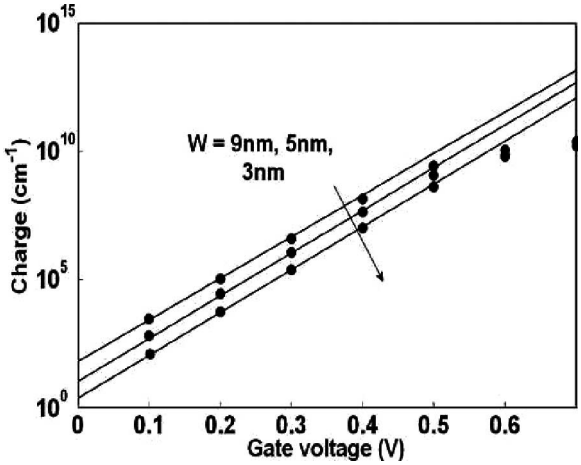

Fig. 4. Variation of quantum integrated charge at virtual cathode with gate voltage for different film width for $H = 9$ nm and $L = 20$ nm. Symbols and lines represent the Atlas simulation and model respectively.

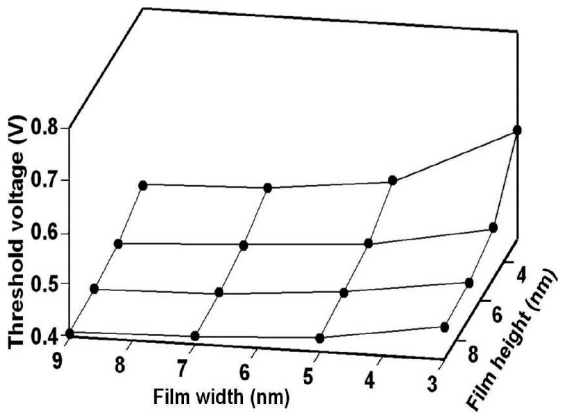

Fig. 5. Variation of quantum threshold voltage with film height and width for channel length ($L = 20$ nm). Symbols and lines represents the Atlas simulation and model, respectively.

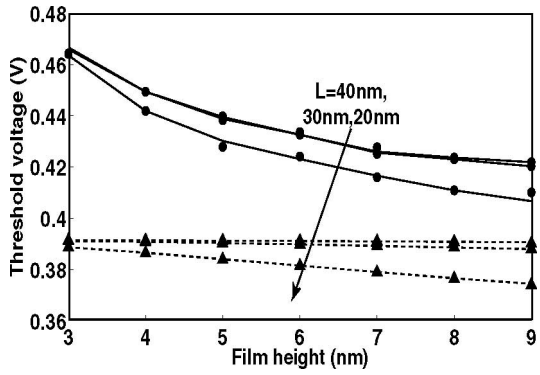

Fig. 6. Variation of threshold voltage with film height for different channel lengths for $W = 9$ nm. Line and circle symbol represents the quantum threshold voltage model and the quantum Atlas simulation. Dashed line and triangle symbol represents the classical threshold voltage model and the Atlas simulation.

sometimes (depending on the device geometry) lies in the strong inversion regime, and thus, overpredict the threshold voltage. In this paper, we first extract the threshold voltage from classical simulation of $I_d - V_g$ characteristics by linear interpolation

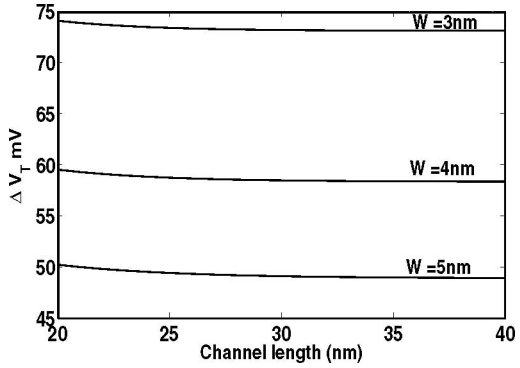

Fig. 7. Variation of ΔV_T with channel length for variuos widths ($H = 9$ nm).

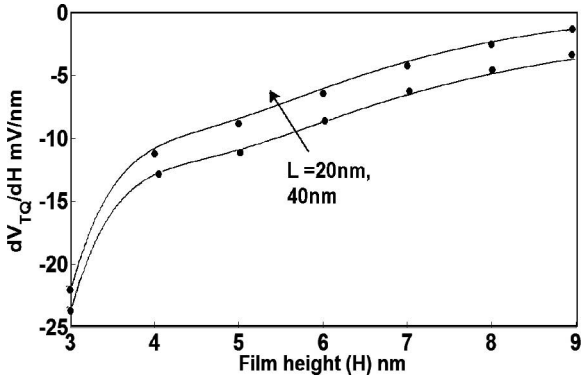

Fig. 8. Variation of $dV_{\rm TQ}/dH$ with film height for different channel lengths. Line and Symbols indicates the variation at $W = 8$ nm and $W = 9$ nm.

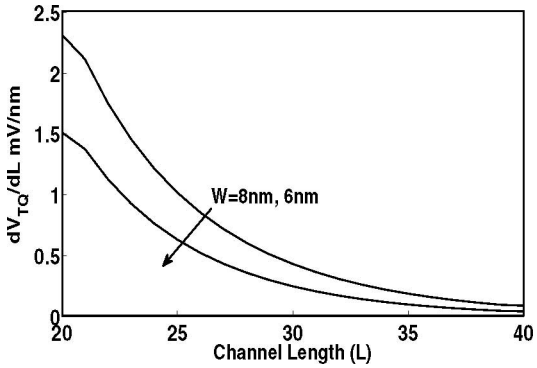

Fig. 9. Variation of $dV_{\rm TQ}/dL$ with channel lengths for different film widths at $H = 9$ nm.

method for wide range of device architectures. Corresponding to the extracted threshold voltage, integrated charge at virtual cathode is computed for each device and an average charge is taken as the threshold charge, which is 5×10^{24} qWHcm^{-1}.

Figs. 8 and 9 show the variation of first derivative of quantum threshold voltage with film height and length, respectively. A quad gate transistor is symmetric about width and height. Hence, the derivative of quantum threshold voltage with respect to channel width also remains almost same as Fig. 8. These figures are obtained by numerically computing the derivatives of quantum threshold voltage obtained from the proposed model. It is seen from the Fig. 8 that the variation is high at lower film

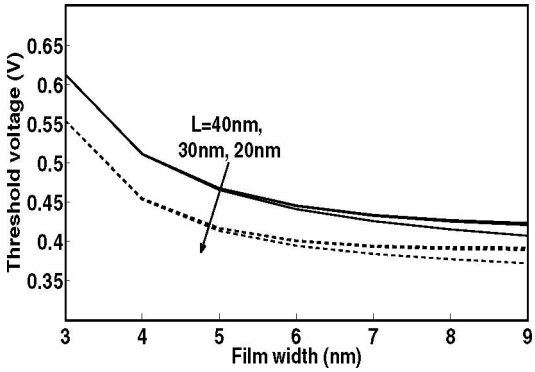

Fig. 10. Variation of threshold voltage with film width for different channel lengths at $H = W$. Line and dashed line represents the quantum threshold voltage with bulk effective mass and modified effective mass m^*.

height compared to higher values, which is due to the quantum confinement effect. The effect of variation of device geometries on the quantum threshold voltage could be obtained by using the chain rule as follows:

$$\frac{\Delta V_{\rm TQ}}{V_{\rm TQ}} = \frac{W}{V_{\rm TQ}}\frac{\delta V_{\rm TQ}}{\delta W}\frac{\Delta W}{W} + \frac{H}{V_{\rm TQ}}\frac{\delta V_{\rm TQ}}{\delta H}\frac{\Delta H}{H} + \frac{L}{V_{\rm TQ}}\frac{\delta V_{\rm TQ}}{\delta L}\frac{\Delta L}{L}. \tag{60}$$

Now, for example, if there is 5% increase in width of the transistor due to process variation for the geometry $W = 9$ nm, $H = 8$ nm, and $L = 20$ nm, using the derivative values from Figs. 8 and 9, we get the following value for $\Delta V_{\rm TQ}$ as:

$$\frac{\Delta V_{\rm TQ}}{V_{\rm TQ}} = -0.0048\frac{\Delta W}{W} - 0.0032\frac{\Delta H}{H} + 0.002316\frac{\Delta L}{L}. \tag{61}$$

If we assume zero variation in channel length, the variation in threshold voltage can be made zero if film height decreases by an amount of 7.5%. In this way in a quad gate MOSFET, the effect of variation in one dimension could be compensated by properly tuning the other dimension.

So far in the discussion, we assumed the value of the effective masses to be equal to the value of bulk silicon effective masses. However, the values of effective masses changes with the device dimensions. For a cylindrical body silicon nanowire transistor, having a diameter d, the effective mass could be formulated as a function of d by following equation [9]:

$$m^*_{l,t}(d) = m^*_{l,t}(\infty)\left(1 + \frac{a_{l,t}}{d} + \frac{b_{l,t}}{d^2}\right) \tag{62}$$

where $a_{l,t}$ and $b_{l,t}$ are the fitting parameters having the values $a_l = 0, a_t = 0.68, b_l = 0.28$, and $b_t = 0.87$. $m^*_{l,t}(\infty)$ denotes the effective mass in bulk silicon. In this paper, we approximated the value of equivalent nanowire diameter to be equal to $(W + H)/2$. In Fig. 10 the lines shows the variation of threshold voltage if we use the constant bulk effective mass and dashed lines shows the variation of threshold voltage if we use effective mass obtained from (62). It is seen from the figure that the threshold voltage is low when we consider the effective mass

dependence on device geometry rather than assuming it to be a constant.

IV. Conclusion

A physically based analytical linear quantum threshold voltage model for a quad gate has been developed and verified as against professional numerical simulator. The proposed model, which is based on the solution of the Poisson and Schrödinger equations does not use any fitting parameters and is capable of predicting the threshold voltage for ultrashort channel and ultrathin body devices.

References

[1] J. P. Colinge, *FinFETs and Other Multi-Gate Transistors*. New York: Springer-Verlag, 2007.

[2] K. Nehari and D. Munteanu, "Compact modeling of the threshold voltage in silicon nanowire MOSFET including 2-D-quantum confinement effects," *Molecular Simul.*, vol. 31, pp. 839–845, Oct. 2005.

[3] *Atlas user manual*, version 5.14.0.R.

[4] X. Liang and Y. Taur, "A 2-D analytical solution for SCEs in DG MOSFEts," *IEEE Trans. Electron Devices*, vol. 51, no. 9, pp. 1385–1391, Sep. 2004.

[5] E. Kreyszig, *Advanced Engineering Mathematics*. New York: Wiley, 2005.

[6] D. J. Griffith, *Introduction to Quantum Mechanics*. Reading, MA: Addison-Wesley, 2004.

[7] D. Munteanu, J. L. Autran, and S. Harrison, "Quantum short channel compact model for the threshold voltage in double gate MOSFETs with high-permittivity gate dielectrics," *J. Non-Crystalline Solids*, vol. 351, pp. 1911–1918, 2005.

[8] M. J. van Dort, P. H. Woerlee, and A. J. Walker, "A simple model for quantisation effects in heavily-doped silicon MOSFETs at inversion conditions," *Solid State Electron.*, vol. 37, no. 3, pp. 411–414, 1994.

[9] E. Gnani, S. Reggiani, M. Rudan, and G. Baccarani, "Effects of the band-structure modification in silicon nanowires with small diameters," in *Proc. Solid State Device Res. Conf.*, 2006, pp. 170–173.

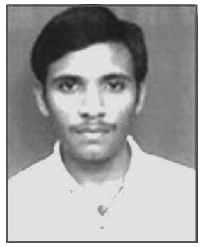

P. Rakesh Kumar received the B.Tech degree in electrical engineering from National Institute of Technology, Kurukshetra, India, in 2007. He is currently working toward the M.Sc. (Engg.) degree with the Nanoscale Device Research Laboratory, Centre for Electronics Design and Technology, Indian Institute of Science, Bangaluru, Karnatka, India.

His current research interests include RF analog circuits, compact modeling, and simulation of semiconductor devices.

Santanu Mahapatra (M'08) received the B.E. degree in electronics and telecommunication from Jadavpur University, Kolkata, India, in 1999, the M.Tech. degree in electrical engineering with specialization in microelectronics from the Indian Institute of Technology, Kanpur, India, in 2001, and the Ph.D. degree in electrical engineering, from the Swiss Federal Institute of Technology Lausanne, Lausanne, Switzerland, in 2005, where he was engaged on compact modeling of single electron transistors and their hybridization with CMOS.

Since 2005, he has been an Assistant Professor with the Nanoscale Device Research Laboratory, Centre for Electronics Design and Technology (CEDT), Indian Institute of Science, Bangaluru, Karnatka, India. He is the founder of the Nanoscale Device Research Laboratory at the CEDT, in 2006, where his team is engaged in research on compact modeling and simulation of emerging nanotechnologies and advanced CMOS devices. He provides consultancy to the device reliability group of Cypress Semiconductor. He is the author and coauthor of several international journals and refereed conferences. He is also the author of the book "Hybrid CMOS Single Electron Transistor Device and Circuit Design" (London, U.K.: Artech House, 2006). His current research interests include device reliability, multigate transistors, tunnel field-effect transistors, single-electron transistors, and CMOS-nanohybridization.

Dr. Mahapatra received the Best Paper Award in the International Semiconductor Conference, Romania, in 2003. He is also the recipient of International Business Machines Corporation Faculty Award, in 2007, Microsoft India Research Outstanding Faculty Award, in 2007, and the Associateship of Indian Academy of Science, in 2009.